Benchmarking solid-to-plasma transition modeling for inertial confinement fusion laser-imprint with a pump-probe experiment

A. Pineau [1,2,*] K. R. P. Kafka [2,*] S. G. Demos,[2,†] T. Z. Kosc,[2] V. N. Goncharov,[2,3] S. X. Hu,[2,3,‡] and G. Duchateau [4,1,§]

[1]*Université de Bordeaux-CNRS-CEA, Centre Lasers Intenses et Applications, UMR 5107, 351 Cours de la Libération, 33405 Talence Cedex, France*

[2]*Laboratory for Laser Energetics, University of Rochester, 250 East River Road, Rochester, New York 14623, USA*

[3]*Department of Mechanical Engineering, University of Rochester, Rochester, New York 14623, USA*

[4]*CEA-CESTA, 15 Avenue des Sablières, CS60001, 33116 Le Barp Cedex, France*

(Received 11 January 2022; accepted 21 July 2022; published 6 September 2022)

For laser direct-drive (LDD) fusion implosions, intense laser beams are used to directly illuminate the inertial confinement fusion (ICF) capsule. The laser beams' intensity nonuniformity (due to speckles) on the target can impose perturbation seeds which are subsequently amplified by Rayleigh-Taylor instability growth, thereby leading to degradation of ICF implosion performance. To devise methods to mitigate this issue, adequate understanding of the underlying so-called laser-imprinting process is required. Here, we report measurements and modeling of the initial plasma formation process which has been shown to affect the laser imprint. Specifically, we measured the transient transmission of a femtosecond probe pulse through a polystyrene target for different 100-picosecond pump pulse intensities pertaining to ICF conditions. The experimental data are used to benchmark a microphysics model of initial plasma formation that overall describes the observed dynamics, thus providing a validated solid-to-plasma modeling for laser-imprinting purposes in radiation-hydrodynamic codes to accurately simulate and design LDD targets.

DOI: 10.1103/PhysRevResearch.4.033178

I. INTRODUCTION

Inertial confinement fusion (ICF) has been actively pursued over the past few decades following the introduction of the concept in 1972 [1]. The most recent progress in creating burning deuterium-tritium (DT) plasmas [2] by the so-called laser indirect-drive (LID) scheme [3] has stimulated renewed excitement on the potential for future applications. In the LID scheme, a capsule consisting of a solid DT-layer covered by ablator materials is being "bathed" by x rays in a laser-driven hohlraum. The LID advantage is that x rays provide a more uniform drive for the ICF target inside the hohlraum, while its disadvantage lies in the low coupling efficiency from laser energy to the kinetic energy of the imploding shell. In contrast, the laser direct-drive (LDD) fusion scheme relies on the direct laser illumination on ICF capsules, which can couple twice the laser energy to the target [4–7]. This can lead to larger margin for ignition and higher gain target designs. With the ultimate goal of developing inertial fusion energy technology, the LDD scheme might be the most promising approach. However, one of the major challenges for LDD is the so-called laser imprinting issue [8–10], that is, the nonuniform laser intensity on the ICF target can imprint pressure and density perturbations that seed the notorious Rayleigh-Taylor instability growth, leading to the failure of LDD implosions [11–15].

To better simulate the laser imprinting effects in LDD, in particular during the early interaction where the initial solid state was shown to play a role [16], one needs to have a reliable physics model to describe how the plasma is formed during the initial tens of picoseconds of the intense laser pulse irradiating an ICF target (such durations correspond to the so-called picket pulses used for target conditioning before the main drive pulse arrives). For the usual dielectric ablator materials such as polystyrene (CH), this initial plasma formation process involves a sequence of processes including multiphoton ionization, plasma formation, free electron laser heating, etc. To the best of our knowledge, almost all of radiation-hydrodynamic codes for LDD have ignored such micro-physics processes in simulating LDD implosions, by assuming a plasma state prior to any laser interaction. Such an oversimplification may have contributed to significant discrepancies between laser-imprinting simulations and experiments [16,17]. The objective of this work is to validate and optimize a microphysics model to enable a more accurate description of processes involved in the initial plasma formation for LDD. This effort adapts concepts previously discussed regarding the laser-induced excitation mechanism [18–21]. Specifically, we present the first laser-imprinting modeling supported by direct experimental results that employed time-resolved optical probing of the dynamics at the onset of plasma formation with adequate temporal and

*These authors contributed equally to this work.
†sdemos@lle.rochester.edu
‡shu@lle.rochester.edu
§guillaume.duchateau@cea.fr

spatial resolution. The experiments involve exposure of CH foils to 100 ps, 355 nm pulses ranging in intensity from about 10^9 to 10^{14} W/cm^2, accompanied by a 250 fs probe pulse that enables acquisition of time-resolved images of the plasma formation process. These results facilitate a better understanding of the dominant physics process behind the initial plasma formation for LDD targets. With such an experiment-benchmarked physics model being implemented into rad-hydro-codes, we will be in a much better position to accurately assess laser imprint effects in LDD and to have trustable modeling tools to develop imprint mitigation strategies [22–28] for the success of LDD.

II. EXPERIMENTAL SETUP AND OBSERVATIONS

The laser system used in this work is a custom-designed optical parametric chirped pulse amplification (OPCPA) system (EKSPLA) providing two output pulses. The first output has a central wavelength at 900 nm, pulse duration of about 20 fs and maximum energy of 2 mJ, while the second output is at 355 nm with a pulse duration of about 100 ps and output maximum pulse energy of about 100 mJ. The 355 nm pulse is obtained by diverting a fraction of the pump laser of the OPCPA system to an amplifier and subsequently generating its third harmonic. Since the two pulses (20 fs and 100 ps) arise from the same pump laser, the jitter between them is very small, estimated to be on the order of 1 ps or less. For the execution of the experiments, the 355-nm pulse (simulating the picket pulse) is focused, with numerical aperture <0.05, into the sample with a variable beam spot, depending on the required laser intensity and experimental conditions. The maximum intensity that can be used for these experiments is $5.\times10^{13}$ W/cm^2. The development and evolution of the plasma process is probed using the second harmonic of the ultrafast laser (generated with a 0.1-mm-thick BBO crystal) after passing through a computer-controlled optical delay line. The duration of the 450 nm probe pulse when reaching the target was measured to be about 250 fs.

The experiments were performed inside a vacuum chamber at a pressure of about 10^{-5} Torr using 30-μm-thick polystyrene films (Goodfellow Corp). The schematic depiction of the experimental setup is shown in Fig. 1(a). The film is held between two metal plates having an array of 9-mm diameter orifices that allow multiple sites on the film to be tested within each orifice [see inset in Fig. 1(a)]. The pump (355 nm, 100 ps) pulse is focused using a 30-cm focal length lens (L). A beam splitter (BS) is used to divert a fraction of the converging beam to image into a beam profiling camera (CCD-1), after undergoing 5X magnification (L-5X), an image plane equivalent to the input surface of the sample. The size of the beam is controlled by moving the position of lens, while the energy of the pulse is controlled from the user interface. The exact temporal profile of the pump pulse is obtained via difference frequency mixing of the pump and probe pulses using a second thin BBO crystal.

Mirrors (M) are used to direct the pump and probe pulses onto the sample as depicted in Fig. 1(a). The probe pulse traverses the area of plasma formation and acts as strobe illumination in a microscope shadowgraph system equipped with a 10X long working distance objective. The image is captured

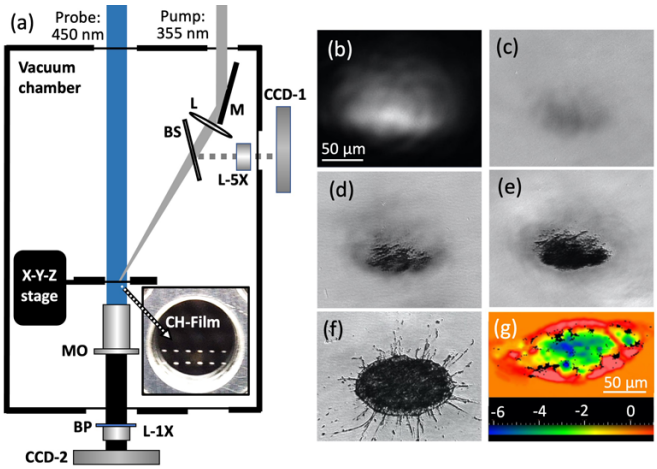

FIG. 1. Schematic diagram of the experimental system (a). The pump beam profile on the target, recorded by CCD-1, for peak intensity of 1.2×10^{11} W/cm^2 is shown in (b). Time resolved microscopic images of the target captured with CCD-2 at delays of −40 ps, 0 ps (peak of pump pulse), +60 ps and 1 s are shown in (c), (d), (e), and (f), respectively. Optical profilometry image of the exposed site (g).

by a CCD camera (CCD-2) after passing through a probe laser bandpass) filter (to eliminate transmission of the pump light and limit collection of plasma emission) and an objective-matching tube lens (L-1X). The plasma formation dynamics is captured by the loss of transmission of the probe pulse as a function of the delay time [29,30]. Example results for experiments performed at a peak intensity of 1.4×10^{11} W/cm^2 are shown in Figs. 1(b)–1(g). Figure 1(b) shows the beam intensity profile on the sample (captured by CCD-1) while Figs. 1(c), 1(d) and 1(e) are time resolved images captured (using CCD-2) during the pump pulse at delays of 40 ps, 0 ps (peak of pump pulse) and +60 ps (at the end of the laser pulse), respectively. Figure 1(f) shows the final image (seconds after the pump pulse) indicating the formation of a shallow crater which was further analyzed using an optical profilometer [Fig. 1(g)] indicating that the depth of the crater is on the order of 4 μm. This is related to the thickness of the superheated material layer due to critical plasma formation. Image processing for data extraction is performed using ImageJ (National Institutes of Health). The transmission data presented for each pump intensity were obtained from the image region corresponding to the peak intensity.

The analyzed transmission data obtained at the location of peak intensity of the pump pulse on the target are shown in Fig. 2 for various laser peak intensities (see caption), preventing in particular from any refraction effect. The material is transparent (transmission close to unity) during the early interaction with the pulse while the intensity is low enough. Later when the plasma forms, i.e., the material is significantly ionized, the transmission drops due to the increase in both absorption and reflection [29–32].

III. MODELING AND DISCUSSION

In order to interpret the experimental data and underlying physical mechanisms of plasma formation, a model has been developed based on the following phenomenological

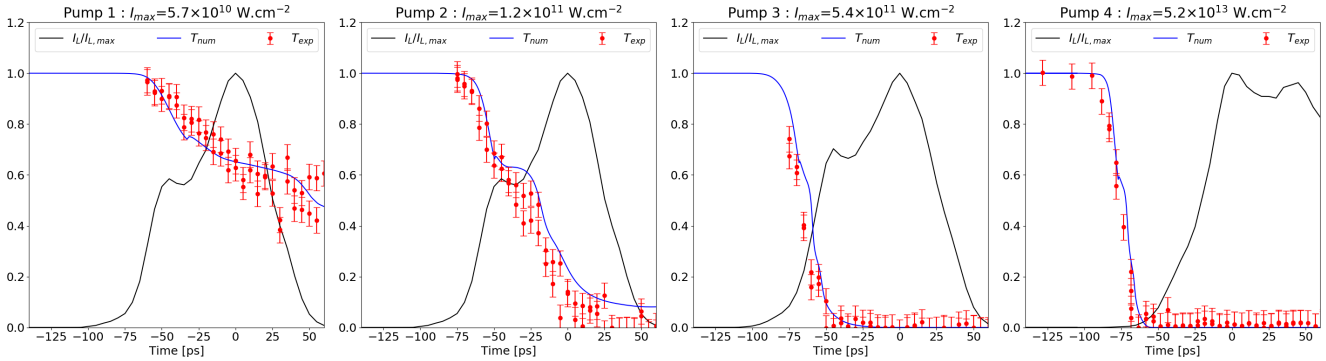

FIG. 2. Evolution of the relative transmission as a function of time for four peak intensities of the laser pump pulse: (a) 5.7×10^{10} W/cm^2, (b) 1.2×10^{11} W/cm^2, (c) 5.4×10^{11} W/cm^2, (d) 5.2×10^{13} W/cm^2. The red dots and the solid blue curve denote the experimental data (with vertical error bars) and modeling results, respectively. The black solid curves depict the normalized pump intensity profile.

description of the solid-to-plasma transition [18]. In the case of polystyrene, which is a dielectric material with a band gap of 4.05 eV, the first interaction stage consists of the material ionization, i.e., electron transition from the valence to the conduction band, through simultaneous absorption of two photons. The excited electrons further absorb photons and transfer energy into the lattice due to collisions with phonons and ions. As a result, both electron and ion temperatures increase leading to further ionization by impact, and phase transitions including the polystyrene fragmentation into monomers, molecules, and atomic species [19,21]. In the same time, free electrons may relax to bound states. The rate of these processes is governed by the laser intensity which is modulated along the propagation direction due to its interaction with the material: the deeper the interaction zone, the lower the local laser intensity due to losses in preceding material.

The first modeling element describes the laser propagation through the target to evaluate the transmission of the probe pulse. Since the laser beam remains mainly collimated during propagation in the target (the target thickness is significantly shorter than the Rayleigh length), the laser intensity variations due to diffraction are neglected. A one-dimensional description in the direction of laser propagation is thus used. Due to the relatively long laser pulse (much longer than an optical cycle), the envelope approximation is used to describe the laser electric field, $E(x,t)$, which then is the solution of Helmholtz equation $\Delta E + k_0^2 \varepsilon E = 0$ [33], where k_0 is the wave vector in vacuum. The evolution of the laser field is driven by the complex permittivity, ε, which depends on the state of matter. The following expression is used [34]:

$$\varepsilon = \varepsilon_{vb} + i\frac{\sigma}{\varepsilon_0 \omega}, \tag{1}$$

where ε_{vb} and the electrical conductivity σ accounts for the contribution of bound and free electrons to the dielectric function, respectively. ω is the laser frequency and ε_0 the vacuum permittivity. To account for the evolution of the matter state from the initial dielectric solid (all electrons are bound) to the full plasma (all electrons are free), we set $\varepsilon_{vb} = 1 + \frac{n_n}{n_t}(\varepsilon_s - 1)$ where n_t and n_n are the total density of all species (neutral and ionic) and density of only neutral species, respectively, which depends on the state of matter. $\varepsilon_s = 2.5$ is the permittivity of the unperturbed solid polystyrene. n_t mainly depends on the ion-lattice temperature T_{il} [19,21] which drives the chemical fragmentation of polystyrene into various molecular and atomic species, leading ultimately to fully ionized carbon and hydrogen atoms [19]. The electrical conductivity is evaluated within the Drude model which has been widely shown efficient to model the optical properties of matter. This approach is a balance between accuracy and numerical efficiency for future coupling with hydrocodes. Within this approach, $\sigma = e^2 n_e / m_e(\nu_c - i\omega)$ where e is the electron charge, m_e is its mass, and ν_c is the collision frequency of electrons with phonons, neutral species, or ions depending on the state of matter. n_e and ν_c are evaluated with the models presented in Refs. [18] and [19], respectively. The last remaining quantities to evaluate are the electron and ion-lattice temperatures which are determined with the two-temperature model presented in Ref. [18]. Note that any diffusion or hydrodynamic process can be neglected within the present laser parameters on a 100 -ps characteristic time [21]. The model is implemented numerically with usual techniques.

Calculations with the previously presented model have been carried out to obtain the temporal evolution of the transient transmission and compare with experimental data. The obtained results are shown in Fig. 2 with four example laser intensities along with the corresponding experimental data. Note that values used for simulations and for the collection of experimental data correspond to the location of peak intensity on the target.

The modeling simulations are in a good agreement with the experimental data: the monotonic decrease with respect to time is captured, and increasing intensity causes a faster decrease rate that is shifted to an earlier onset time. Also the transmission does not fully drop to zero for the two lowest intensities. The fitting was performed by varying the smallest number of model parameters as the assurance of reliability of our modeling, finally leading to adjustment of only two parameters: the multiphoton ionization rate (evaluated with the Keldysh expression) and the electron relaxation time. The photoionization rate is weighted by a factor of 0.5, and the relaxation time is set to 1 ns. The possibility of adjusting the Keldysh expression is justified by the fact it has been derived with various assumptions including an ideal shape of the band structure. Regarding the relaxation time, it is

significantly longer than the value of 1 ps used in Ref. [18] which corresponds to the time scale of the electron dynamics in the pure solid state. Since the latter state is left early during the interaction (low melting point of polystyrene), a plasma at solid density (not fully ionized) is the representative state of matter during the whole interaction, for which the characteristic electron relaxation time scale lies in the nanosecond range [35,36]. Since our model includes only a single variable to describe relaxation (for multiscale purpose of efficient introduction in hydrocodes), it accounts for this time-average representative state of matter, i.e., the plasma state.

By analyzing the physical quantities provided by the simulations, the observed behaviors may be interpreted as follows. During the early interaction with low enough intensity, the material is transparent because absorption is nonlinear due to the first interaction stage of simultaneous absorption of two photons to ionize the material. The general monotonic decrease in the transmission is mainly related to the production of free electrons, their density increasing monotonically as a function of delay time. When the free electron density is in excess of roughly the critical density (at the probe wavelength), the transmission drops (the evolution of the electron density in space is shown and discussed later). The higher the intensity, the earlier the efficient production of free electrons occurs, which explains the onset of transmission loss shifting to earlier delay times. Furthermore, the rate of transmission decline also increases as a function of the laser peak intensity. For the higher intensities (pump-2,-3 and -4), the final free electron density is in excess of the critical density and the probe beam transmission drops to zero during the pump pulse. For the lower intensity case (pump-1), the final maximum density is subcritical, of 5.5×10^{19} cm^{-3}, leading to a final transmission of ∼50%.

The present modeling provides a better understanding of how the laser absorption and the subsequent solid-to-plasma transition take place in the bulk material by monitoring the temporal evolution of the free electron density and temperature in space. Figure 3 shows the evolution of the free electron density with respect to the sample depth and delay time for pump intensities I_1 and I_3 (for the sake of conciseness, temperatures are not shown, they exhibit a similar shape as electron density). For the lowest intensity I_1, the maximum electron density at the end of the interaction is $\sim5.\times10^{19}$ cm^{-3} which is significantly smaller than the critical plasma density. The laser pulse then propagates along the whole target depth, leading to a rather homogeneous free electron production of the order of 10^{19} cm^{-3} (low-density plasma), and thus low absorption. By increasing the laser intensity, the rate of electron/plasma density growth is enhanced, increasing both absorption and reflection (therefore decreasing transmission). As the laser propagates inside the material, the intensity decreases with propagation distance. This behavior can be observed in Fig. 3(b) where the matter is fully ionized on the sample surface ($n_e = 3.5\times10^{23}$ cm^{-3}), but has a significant decrease of the electron density with depth. This decrease has an exponential-like shape over a distance of ∼10 μm, characterizing an attenuation depth, beyond which the laser intensity is low enough to retrieve conditions of Fig. 3(a) where all quantities become rather homogeneous. This attenuation depth is inversely related to the laser intensity. For I_2 and I_4, it is ∼15 μm and ∼10 μm at the end of the pulse, respectively. Considering the depth where the electron density is overcritical, leading to strong laser absorption and material ejection, it is in the micrometric range which is comparable with the experimentally observed depth of craters [see Fig. 1(g)] . It is the same for both I_3 and I_4 intensities because the fully ionized state at the surface is reached well before the interaction ends. Note that the attenuation depth becomes shorter over the course of the interaction, going from the whole sample thickness to the previously mentioned values. In the attenuation depth area, the electron density is large enough to induce significant absorption. Therefore, the target is expected to undergo the initiation of solid-to-plasma transition at the sample surface whereas, roughly above the attenuation depth, the material remains relatively cold and in the solid state (during the laser pulse).

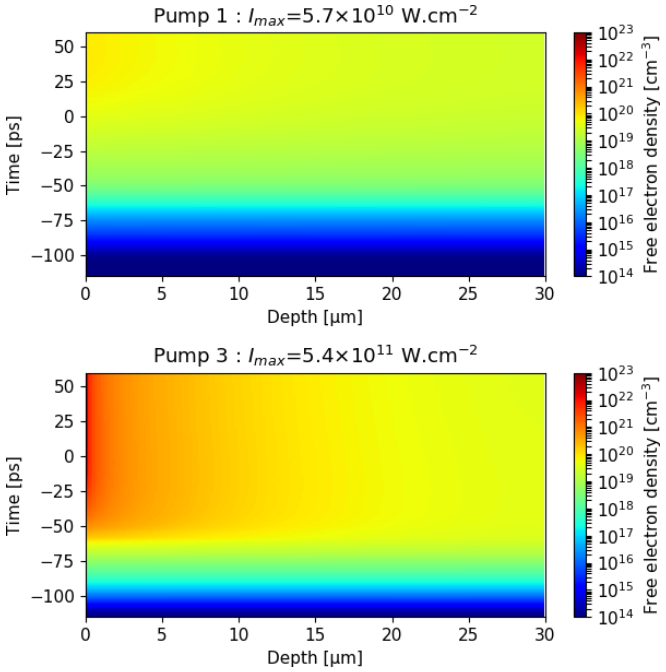

FIG. 3. Evolution of the free electron density (in units of cm^{-3}) as a function of depth and time for (a) $I_1 = 5.7\times10^{10}$ W/cm^2 and (b) $I_3 = 5.4\times10^{11}$ W/cm^2.

IV. CONCLUSION

In conclusion, a pump-probe experiment to measure the transient transmission of a 100-ps laser pulse, pertaining to a ICF-LDD picket or the early rise of a drive pulse, has been developed. The transmission accounts for the plasma formation in a dielectric material, evolving from unity to zero, whose dynamics have been observed to depend on the laser peak intensity. Our modeling of solid-to-plasma transition, predicting the laser induced transient optical properties of matter, is in very good agreement with these experimental observations. This agreement was obtained by adjusting the multiphoton ionization rate and the electron relaxation time to consider an "average" value during the rapid change of the material state. The electron dynamics driven by photoabsorption and material phase transitions has been shown to

mainly drive the transmission evolution. The present work thus benchmarks this plasma formation stage, and paves the way for its introduction in three-dimensional hydrocode for accurately simulating both the laser imprint and shine-through issues [37]. This capability can help advance target and/or drive system designs to minimizing the formation of hydrodynamic instabilities, and thus optimize the ICF implosion yield.

ACKNOWLEDGMENTS

Work done by LLE is supported by the Department of Energy National Nuclear Security Administration under Award No. DE-NA0003856, the University of Rochester, and the New York State Energy Research and Development Authority.

This report was prepared as an account of work sponsored by an agency of the U.S. Government. Neither the U.S. Government nor any agency thereof, nor any of their employees, makes any warranty, express or implied, or assumes any legal liability or responsibility for the accuracy, completeness, or usefulness of any information, apparatus, product, or process disclosed, or represents that its use would not infringe privately owned rights. Reference herein to any specific commercial product, process, or service by trade name, trademark, manufacturer, or otherwise does not necessarily constitute or imply its endorsement, recommendation, or favoring by the U.S. Government or any agency thereof. The views and opinions of authors expressed herein do not necessarily state or reflect those of the U.S. Government or any agency thereof.

[1] J. Nuckolls *et al.*, Laser compression of matter to super-high densities: Thermonuclear (CTR) applications, Nature (London) **239**, 139 (1972).

[2] A. B. Zylstra, O. A. Hurricane, D. A. Callahan *et al.*, Burning plasma achieved in inertial fusion, Nature **601**, 542 (2022).

[3] J. Lindl, Development of the indirect-drive approach to inertial confinement fusion and the target physics basis for ignition and gain, Phys. Plasmas **2**, 3933 (1995).

[4] V. N. Goncharov, S. P. Regan, E. M. Campbell, T. C. Sangster, P. B. Radha, J. F. Myatt, D. H. Froula, R. Betti, T. R. Boehly, J. A. Delettrez *et al.*, National direct-drive program on OMEGA and the National Ignition Facility, Plasma Phys. Controlled Fusion **59**, 014008 (2017).

[5] S. X. Hu, R. Epstein, W. Theobald, H. Xu, H. Huang, V. N. Goncharov, S. P. Regan, P. W. McKenty, R. Betti, E. M. Campbell *et al.*, Direct-drive double-shell implosion: A platform for burning-plasma physics studies, Phys. Rev. E **100**, 063204 (2019).

[6] R. H. H. Scott, K. Glize, L. Antonelli, M. Khan, W. Theobald, M. Wei, R. Betti, C. Stoeckl, A. G. Seaton, T. D. Arber *et al.*, Shock Ignition Laser-Plasma Interactions in Ignition-Scale Plasmas, Phys. Rev. Lett. **127**, 065001 (2021).

[7] B. Canaud and M. Temporal, High-gain shock ignition of direct-drive ICF targets for the Laser Mégajoule, New J. Phys. **12**, 043037 (2010).

[8] S. E. Bodner, Rayleigh-Taylor Instability and Laser-Pellet Fusion, Phys. Rev. Lett. **33**, 761 (1974).

[9] R. Ishizaki and K. Nishihara, Propagation of a Rippled Shock Wave Driven by Nonuniform Laser Ablation, Phys. Rev. Lett. **78**, 1920 (1997).

[10] R. Ishizaki and K. Nishihara, Model of hydrodynamic perturbation growth in the start-up phase of laser implosion, Phys. Rev. E **58**, 3744 (1998).

[11] P. B. Radha, T. J. B. Collins, J. A. Delettrez, Y. Elbaz, R. Epstein, V. Y. Glebov, V. N. Goncharov, R. L. Keck, J. P. Knauer, J. A. Marozas *et al.*, Multidimensional analysis of direct-drive, plastic-shell implosions on OMEGA, Phys. Plasmas **12**, 056307 (2005).

[12] S. X. Hu, P. B. Radha, J. A. Marozas, R. Betti, T. J. B. Collins, R. S. Craxton, J. A. Delettrez, D. H. Edgell, R. Epstein, V. N. Goncharov *et al.*, Neutron yield study of direct-drive, low-adiabat cryogenic D2 implosions on OMEGA laser system, Phys. Plasmas **16**, 112706 (2009).

[13] S. X. Hu, V. N. Goncharov, P. B. Radha, J. A. Marozas, S. Skupsky, T. R. Boehly, T. C. Sangster, D. D. Meyerhofer, and R. L. McCrory, Two-dimensional simulations of the neutron yield in cryogenic deuterium-tritium implosions on OMEGA, Phys. Plasmas **17**, 102706 (2010).

[14] S. X. Hu, D. T. Michel, A. K. Davis, R. Betti, P. B. Radha, E. M. Campbell, D. H. Froula, and C. Stoeckl, Understanding the effects of laser imprint on plastic-target implosions on OMEGA, Phys. Plasmas **23**, 102701 (2016).

[15] D. T. Michel, S. X. Hu, A. K. Davis, V. Y. Glebov, V. N. Goncharov, I. V. Igumenshchev, P. B. Radha, C. Stoeckl, and D. H. Froula, Measurement of the shell decompression in direct-drive inertial-confinement-fusion implosions, Phys. Rev. E **95**, 051202(R) (2017).

[16] J. L. Peebles, S. X. Hu, W. Theobald, V. N. Goncharov, N. Whiting, P. M. Celliers, S. J. Ali, G. Duchateau, E. M. Campbell, T. R. Boehly *et al.*, Direct-drive measurements of laser-imprint-induced shock velocity nonuniformities, Phys. Rev. E **99**, 063208 (2019).

[17] J. Oh, A. J. Schmitt, M. Karasik, and S. P. Obenschain, Measurements of laser-imprint-induced shock velocity nonuniformities in plastic targets with the Nike KrF laser, Phys. Plasmas **28**, 032704 (2021).

[18] G. Duchateau, S. X. Hu, A. Pineau, A. Kar, B. Chimier, A. Casner, V. Tikhonchuk, V. N. Goncharov, P. B. Radha, and E. M. Campbell, Modeling the solid-to-plasma transition for laser imprinting in direct-drive inertial confinement fusion, Phys. Rev. E **100**, 033201 (2019).

[19] A. Pineau, B. Chimier, S. X. Hu, and G. Duchateau, Modeling the electron collision frequency during solid-to-plasma transition of polystyrene ablator for direct-drive inertial confinement fusion applications, Phys. Plasmas **27**, 092703 (2020).

[20] A. Kar, S. X. Hu, G. Duchateau, J. Carroll-Nellenback, and P. B. Radha, Implementing a microphysics model in hydrodynamic simulations to study the initial plasma formation in dielectric ablator materials for direct-drive implosions, Phys. Rev. E **101**, 063202 (2020).

[21] A. Pineau, B. Chimier, S. X. Hu, and G. Duchateau, Improved modeling of the solid-to-plasma transition of polystyrene ablator for laser direct-drive inertial confinement fusion hydrocodes, Phys. Rev. E **104**, 015210 (2021).

[22] R. G. Watt, J. Duke, C. J. Fontes, P. L. Gobby, R. V. Hollis, R. A. Kopp, R. J. Mason, D. C. Wilson, C. P. Verdon, T. R. Boehly

et al., Laser Imprint Reduction Using a Low-Density Foam Buffer as a Thermal Smoothing Layer at 351-nm Wavelength, Phys. Rev. Lett. **81**, 4644 (1998).

[23] S. Fujioka, A. Sunahara, K. Nishihara, N. Ohnishi, T. Johzaki, H. Shiraga, K. Shigemori, M. Nakai, T. Ikegawa, M. Murakami *et al.*, Suppression of the Rayleigh-Taylor Instability due to Self-Radiation in a Multiablation Target, Phys. Rev. Lett. **92**, 195001 (2004).

[24] S. Depierreux, C. Labaune, D. T. Michel, C. Stenz, P. Nicolaï, M. Grech, G. Riazuelo, S. Weber, C. Riconda, V. T. Tikhonchuk *et al.*, Laser Smoothing and Imprint Reduction with a Foam Layer in the Multikilojoule Regime, Phys. Rev. Lett. **102**, 195005 (2009).

[25] L. Masse, Stabilizing Effect of Anisotropic Thermal Diffusion on the Ablative Rayleigh-Taylor Instability, Phys. Rev. Lett. **98**, 245001 (2007).

[26] S. X. Hu, G. Fiksel, V. N. Goncharov, S. Skupsky, D. D. Meyerhofer, and V. A. Smalyuk, Mitigating Laser Imprint in Direct-Drive Inertial Confinement Fusion Implosions with High-*Z* Dopants, Phys. Rev. Lett. **108**, 195003 (2012).

[27] G. Fiksel, S. X. Hu, V. A. Goncharov, D. D. Meyerhofer, T. C. Sangster, V. A. Smalyuk, B. Yaakobi, M. J. Bonino, and R. Jungquist, Experimental reduction of laser imprinting and Rayleigh-Taylor growth in spherically compressed, medium-Z-doped plastic targets, Phys. Plasmas **19**, 062704 (2012).

[28] M. Karasik, J. L. Weaver, Y. Aglitskiy, J. Oh, and S. P. Obenschain, Suppression of Laser Nonuniformity Imprinting Using a Thin High-*Z* Coating, Phys. Rev. Lett. **114**, 085001 (2015).

[29] X. Mao, S. S. Mao, and R. E. Russo, Imaging femtosecond laser-induced electronic excitation in glass, Appl. Phys. Lett. **82**, 697 (2003).

[30] S. G. Demos, R. A. Negres, R. N. Raman, A. M. Rubenchik, and M. D. Feit, Material response during nanosecond laser induced breakdown inside of the exit surface of fused silica, Laser Photon. Rev. **7**, 444 (2013).

[31] P. Balling and J. Schou, Femtosecond-laser ablation dynamics of dielectrics: Basics and applications for thin films, Rep. Prog. Phys. **76**, 036502 (2013).

[32] S. Winkler, Transient response of dielectric materials exposed to ultrafast laser radiation, Appl. Phys. A **84**, 413 (2006).

[33] J. D. Jackson, *Classical Electrodynamics*, 3rd ed. (Wiley, New York, 1999).

[34] E. G. Gamaly and A. V. Rode, Transient optical properties of dielectrics and semiconductors excited by an ultrashort laser pulse, J. Opt. Soc. Am. B **31**, C36 (2014).

[35] L. Jiao, B. S. Truscott, H. Liu, M. N. R. Ashfold, and H. Ma, Imaging spectroscopy of polymer ablation plasmas for laser propulsion applications, J. Appl. Phys. **121**, 013303 (2017).

[36] L. J. Basile, Effect of styrene monomer on the fluorescence properties of polystyrene, J. Chem. Phys. **36**, 2204 (1962).

[37] D. H. Edgell, W. Seka, R. E. Bahr, T. R. Boehly, and M. J. Bonino, Effectiveness of silicon as a laser shinethrough barrier for 351-nm light, Phys. Plasmas **15**, 092704 (2008).